Dynamics of collective-dephasing-induced multiatom entanglement

Y. Li ⬤,* Y. Mei ⬤,*,† H. Nguyen ⬤, P. R. Berman, and A. Kuzmich
Department of Physics, University of Michigan, Ann Arbor, Michigan 48109, USA

Atomic Rydberg interactions allow one to create atom-light entanglement that can be used for diverse applications in quantum information science. The interaction-induced dephasing of collective atomic states is often the dominant contribution to the entanglement generation process in atomic ensembles. Although the mechanism has been used widely, its dynamics has not been previously observed, while its consequences have sometimes been ascribed instead to the presence of the excitation blockade. Here we report a study of the temporal evolution of an initially unentangled Rydberg spin wave into an (entangled) Dicke state. By comparing our observations to results of numerical simulations, we elucidate how the interaction-induced dephasing is responsible for entanglement generation in many-atom settings. These results have relevance to broad classes of applications for collective atomic systems, including driving of collective atomic qubits, on-demand generation of single photons, and preparation of entangled states involving atoms or light.

Rydberg interactions of atomic qubits provide a compelling platform for the development of quantum computation and simulation hardware [1–6]. The action of two-qubit quantum gates in these approaches is usually explained in terms of the Rydberg blockade mechanism [1,7], where the presence of an excited Rydberg atom blocks nearby atoms from being excited. Such a picture of the blockade mechanism is not strictly correct for an ensemble. This is most easily seen by considering two atoms that have a large Rydberg-Rydberg interaction. In a molecular basis and for an incident field that is resonant with the Rydberg transition in an isolated atom, the single-atom excitation state is resonant, whereas the doubly excited state is shifted out of resonance. Thus, a single atom is never excited in this scheme, only a single excitation shared by the two atoms. For N atoms, the molecular picture remains valid, even if the level scheme becomes very complicated. Related approaches in quantum information protocols employing collective addressing of atomic ensembles [7–13] can be and are typically analyzed in terms of the excitation blockade.

The dipole blockade can also be understood in terms of the individual atom basis. Each pair of excited atoms (j, j') experiences a level shift $\Delta_{jj'}$ that depends on their separation. As long as these level shifts are large in magnitude compared with the bandwidth of the excitation pulse, there will be only a small probability that a double excitation can occur. In principle, the excitation dipole blockade can produce a collective single excitation with unit probability [1,7]. On the other hand, Bariani *et al.* proposed a spin-wave dephasing mechanism in order to achieve much the same goals [14] and this approach has been used to describe generation of quantum light and atom-light entanglement in various experiments [15–19]. In this approach, a short excitation pulse creates a

multiple-excitation state. Following the excitation, all but the singly excited state decay as a result of the distribution of the $\Delta_{jj'}$. If the $\Delta_{jj'}$ were all equal there would be no decay. In effect, the dephasing mechanism exploits interaction-induced phase factors to isolate the singly excited component in the directional (phase-matched) optical retrieval process.

It is important to distinguish between the value of $g_{atoms}^{(2)}(0)$, which is used often as a measure of the efficiency of the dipole blockade, and the value of $g^{(2)}(0)$ associated with the fields radiated in the phase-matched direction following the readout pulse used in our experiment. The value of $g_{atoms}^{(2)}(0)$ is determined by the excitation pulse and does not change during the storage period since it depends only on Rydberg level populations, which are approximately constant during the storage period. On the other hand, $g^{(2)}(0)$ is further reduced during the storage period owing to dephasing. Immediately following the excitation pulse, you might think that $g^{(2)}(0) = g_{atoms}^{(2)}(0)$, but this is not necessarily the case. As a result of the manner in which dephasing affects each of these quantities, one finds that $g^{(2)}(0) < g_{atoms}^{(2)}(0)$ when the blockade mechanism is operative in the excitation phase. In other words, dephasing plays an important role in quantum information protocols involving Rydberg atoms.

If interactions can be neglected in the excitation process, the atoms are prepared in a factorized state, for which the maximum population of a single collective excitation state produced via the dephasing mechanism in the storage period is limited to $1/e$ [14]. In contrast, the Rydberg excitation blockade, in principle, allows one to reach unity efficiency of the collective single excitation [1,7,20,21]. However, in experiments where the prepared atomic state is intended to be mapped into a light field, the efficiency of the mapping is just as important as the atomic state preparation efficiency. The mapping efficiency is a function of cooperativity parameter C (for cavity settings) or, for free-space settings, optical depth d, which for an atomic sample of length L scales

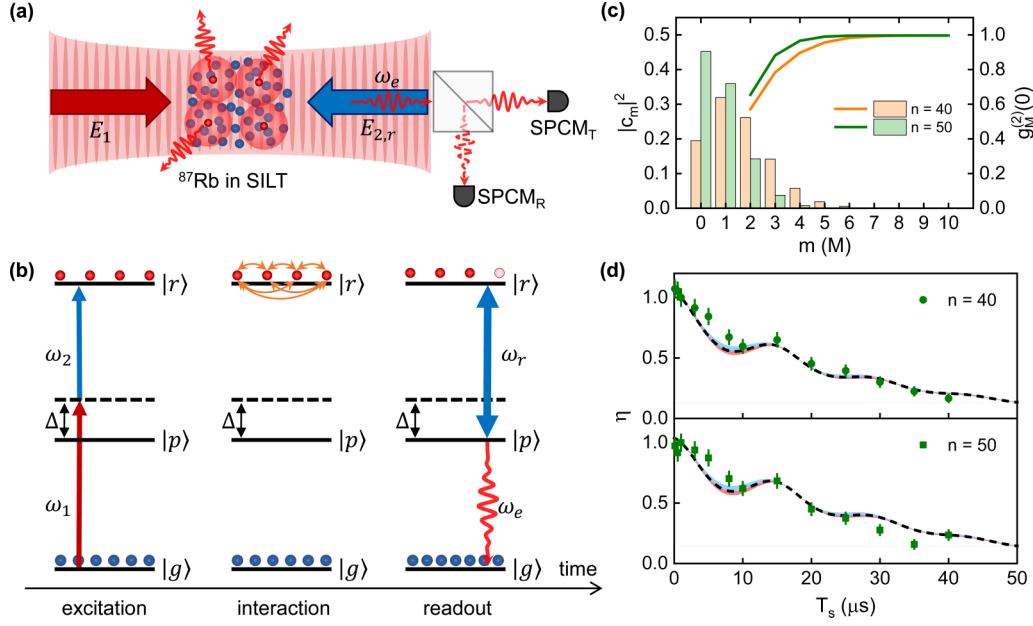*These authors contributed equally to this work.
†meiyf@umich.edu

FIG. 1. (a) Experimental setup. Excitation pulses E_1 (780 nm) and E_2 (480 nm) drive a lattice-confined ^{87}Rb atomic ensemble from $|g\rangle$ to $|p\rangle$ and from $|p\rangle$ to $|r\rangle$, respectively. A retrieval pulse E_r leads to phase-matched emission coupled into a pair of single-mode fibers and subsequently measured by single-photon counting modules $SPCM_T$ and $SPCM_R$. (b) Excitation, interaction, and readout process in the atomic ensemble. The single-atom energy levels for ^{87}Rb are $|g\rangle = |5S_{1/2}, F = 2, m_F = -2\rangle$, $|p\rangle = |5P_{3/2}, F = 3, m_F = -3\rangle$, and $|r\rangle = |nS_{1/2}, m_J = -1/2\rangle$. (c) Histogram bars (left y axis) show the distribution of $|c_m|^2$ for principal quantum numbers $n = 40$ (orange) and $n = 50$ (green). The solid lines (right y axis) show the autocorrelation function $g_M^{(2)}(0)$ as a function of truncation to a maximum of M excitations. (d) Normalized signal η as a function of storage time T_s for principal quantum numbers $n = 40$ (circles) and $n = 50$ (squares). The storage efficiency is normalized to that at 1 μs, where the efficiency is 0.16% and 0.27% for $n = 40$ and 50, respectively. Blue and red bands represent temperatures 25% lower and higher than the best-fit value, respectively.

as approximately $\rho\lambda^2 L$. To achieve near-unity atom-light mapping, the condition $d \gg 1$ must be achieved, which implies $L \gg (\rho\lambda^2)^{-1}$. The atomic density ρ in turn must be kept sufficiently low (in practice, less than or equal to 10^{12} cm^{-3}) so that the rate of ground-Rydberg decoherence is not prohibitive. Taken together, these considerations set such limits on the size and the density of the atomic sample. Thus, regardless of the values of $g_{atoms}^{(2)}(0)$ produced by the excitation blockade, interaction-induced dephasing in both the excitation and storage phases can lead to a value of $g^{(2)}(0)/g_{atoms}^{(2)}(0) \ll 1$. As a consequence, interaction-induced dephasing is an important mechanism for the reduction of $g^{(2)}(0)$ and for entanglement generation.

The major thrust of this paper is an examination of the dynamics for the interaction-induced dephasing. In order to isolate the role of the dephasing, we excite our ensemble with an excitation pulse whose bandwidth is sufficiently large to ensure that the excitation dipole blockade mechanism is inoperative. Following excitation, we are able to follow the dephasing dynamics that reduces the contributions to the signal from the multiply excited states. Thermal motional and collisional dephasing reduce the ground-Rydberg coherence, making it difficult to exploit the timely evolution of Rydberg interactions in an atomic ensemble. We confine the ensemble in a state-insensitive (for the ground and Rydberg atomic states) optical lattice [12,22–24] to achieve up to a 30-μs-long ground-Rydberg coherence time, which allows us to study

the dynamics of interaction-induced dephasing. To study the effect of the dynamic dephasing mechanism, we measure the value of the zero-time second-order autocorrelation function $g^{(2)}$ associated with phase-matched emission from the sample as a function of storage (interaction) times ranging from 0.1 to 25 μs. We observe a fast decrease of $g^{(2)}$ from 1 to 0 for low principal quantum numbers, i.e., $n = 40$ and 50, indicating an evolution from an unentangled Rydberg spin wave into an entangled Dicke state. We confirm that the Rydberg blockade effect plays little role in the dephasing process. The measurements agree well with a theory that accounts for the phase shifts resulting from multiple Rydberg excitations and Rydberg atom–Rydberg atom interactions.

The experimental setup and methods shown in Fig. 1(a) have been described in Ref. [12]. An ultracold ^{87}Rb atomic ensemble is first formed in a magneto-optical trap (MOT) and then loaded to a crossed far-off-resonance dipole trap (FORT) formed by two intersected focused yttrium aluminum garnet laser beams. The atoms are then transferred to a one-dimensional state-insensitive optical lattice trap (SILT) formed by a 1012-nm retroreflected beam. We shine two laser fields E_1 (780 nm, $\sigma-$) and E_2 (480 nm, $\sigma+$), with beam waists $w_{E_1,0} = 6$ μm and $w_{E_2,0} = 15$ μm, to excite atoms from the ground state $|g\rangle = |5S_{1/2}, F = 2, m_F = -2\rangle$ to the Rydberg state $|r\rangle = |nS_{1/2}, m_J = -1/2\rangle$ with a detuning of $\Delta/2\pi = 480$ MHz from the intermediate state $|p\rangle = |5P_{3/2}, F = 3, m_F = -3\rangle$, as shown in Fig. 1(b).

The excitation fields E_1 and E_2 drive the $|g\rangle$-to-$|p\rangle$ and the $|p\rangle$-to-$|r\rangle$ transition with Rabi frequency Ω_1 and Ω_2, respectively.

The ground state of the atomic ensemble is a product state $|\mathbf{0}\rangle = |g_1, \ldots, g_N\rangle$. At the end of the excitation pulse of time T_p ["excitation" in Fig. 1(b)], the atomic state of the ensemble can be approximated by the state $|\Psi_0\rangle = \sum_{m=0}^{N} c_m |\mathbf{m}\rangle$. Here $|\mathbf{m}\rangle$ is the Fock state of m excitations given by $|\mathbf{m}\rangle = \frac{(\hat{S}_{\mathbf{k}_0}^\dagger)^m}{m!} |\mathbf{0}\rangle$ and c_m is given by $c_m = \sqrt{\binom{N}{m}} a^{N-m} b^m$, where $a = \cos\frac{\Omega_1\Omega_2}{4\Delta} T_p$, $b = i \sin\frac{\Omega_1\Omega_2}{4\Delta} T_p$, and $\binom{N}{m}$ is the binomial coefficient. We define the collective excitations of level $|r\rangle$ in terms of spin waves, whose destruction operator is given by $\hat{S}_{\mathbf{k}_0} = \frac{1}{\sqrt{N}} \sum_{\mu=1}^{N} e^{i\mathbf{k}_0 \cdot \mathbf{r}_\mu} \hat{\sigma}_\mu^{gr}$, with $\mathbf{r}_\mu$ the position of atom μ and $\mathbf{k}_0$ the wave vector associated with the excitation. The transition between $|g\rangle$ and $|r\rangle$ is described by the single-particle operators $\hat{\sigma}_\mu^{gr} = |g_\mu\rangle\langle r_\mu|$. We use $\Omega_1/2\pi = 9.2$ MHz, $\Omega_2/2\pi = 25.7 \, (17.9)$ MHz for $n = 40 \, (50)$, $T_p = 103(4)$ ns, and $N \approx 270$; hence the average number of Rydberg excitation is $\bar{m} = bN = 1.63 \, (0.79)$. We plot the distribution of $|c_m|^2$ in Fig. 1(c), from which it can be concluded that nonnegligible values of $|c_m|^2$ occur for $m > 2$.

A controllable delay T_s is applied following the excitation pulse in order to probe Rydberg-Rydberg interactions ["interaction" in Fig. 1(b)]. We utilize the SILT, where the magic detuning condition is satisfied to trap both the ground-state and the Rydberg state atoms [12]. The measured storage efficiency η as a function of storage period T_s is shown in Fig. 1(d). It indicates that for principal quantum numbers $n = 40$ and 50 the lifetime of the ground-Rydberg coherence can be extended up to approximately $30 \, \mu$s for trap depth less than or equal to $30 \, \mu$K. The oscillations result from the nearly periodic motion of the atoms along the optical lattice. The oscillation visibility decreases with time owing to the anharmonic nature of the potential.

For the Rydberg interaction Hamiltonian $\hat{H}_c = \sum_{\mu<\nu} \hbar\kappa_{\mu\nu} \hat{\sigma}_\mu^{rr} \hat{\sigma}_\nu^{rr}$, the state evolution operator can be written as $\hat{U} = \exp(-i\hat{H}T_s/\hbar) = \prod_{\mu<\nu}[1 + \hat{\sigma}_\mu^{rr} \hat{\sigma}_\nu^{rr}(e^{-i\Phi_{\mu\nu}} - 1)]$. From here on we write atomic product states listing only those atoms excited out of their single-atom ground states. For example, $|\mu_1\mu_2\cdots\mu_m\rangle = |g_1\cdots r_{\mu_1}\cdots r_{\mu_2}\cdots r_{\mu_m}\cdots g_N\rangle$ represents m excitations at atom $\mu_1, \mu_2, \ldots, \mu_m$. The two-excitation state after the evolution can be expressed as $\hat{U}|\mu_1\mu_2\rangle = e^{-i\Phi_{\mu_1\mu_2}}|\mu_1\mu_2\rangle$, where $\Phi_{\mu\nu} = \kappa_{\mu\nu}T_s = [\delta/2 - \text{sgn}(\delta)\sqrt{(\delta/2)^2 + V_{\mu\nu}^2}]T_s/\hbar$ is the interaction-induced phase shift on the atom pair during the storage time T_s, with $V_{\mu\nu} = C_3/R_{\mu\nu}^3$ being the dipole-dipole interaction between the pair of atoms and $\delta = E_{r_1} + E_{r_2} - 2E_r$ being the energy defect between the pair state $|rr\rangle$ and the state $|r_1 r_2\rangle$ [14,25,26]. The m-excitation state after the evolution can be thus expressed as $\hat{U}|\mathbf{m}\rangle = \sum_{\mu_1<\cdots<\mu_m} \frac{1}{\sqrt{\binom{N}{m}}} e^{-i\Phi_{\mu_1\cdots\mu_m}}|\mu_1\cdots\mu_m\rangle$, with $\Phi_{\mu_1\cdots\mu_m} = \sum_{1\leqslant i<j\leqslant m} \Phi_{\mu_i\mu_j}$ for $m \geqslant 2$.

Subsequently, a readout pulse E_r (with Rabi frequency of Ω_r) that is on resonance with the $|r\rangle$-to-$|p\rangle$ transition is used to retrieve the phase-matched emission ["readout" in Fig. 1(b)]. The emitted phase-matched photons are then split by a beam splitter and directed into two single-mode optical fibers coupled to the single-photon-counting modules (SPCMs), forming a Hanbury Brown–Twiss (HBT) setup.
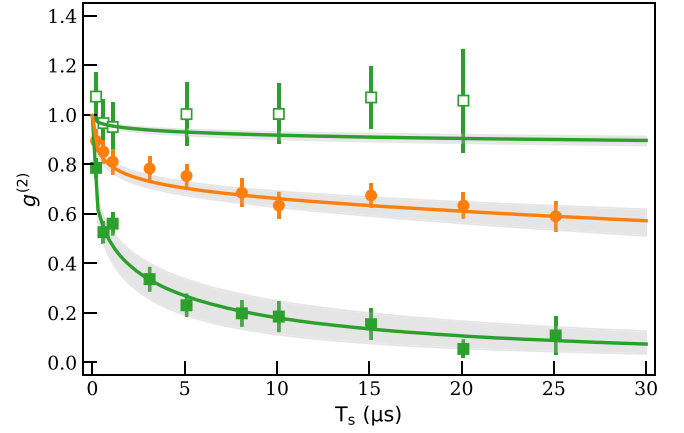

FIG. 2. Dynamic $g^{(2)}$ as a function of interaction time T_s for varying interaction strength: (i) that with same atomic distribution $\sigma_z = 10.5 \, \mu$m but different principal quantum number $n = 40$ (orange closed circles) and $n = 50$ (green closed squares) and (ii) that with same principal quantum number $n = 50$ but different atomic distributions $\sigma_z = 10.5 \, \mu$m (green closed squares) and $\sigma_z = 230 \, \mu$m (green open squares). The solid line is the result of the numerical simulation together with 20% of σ_z (shaded area).

The emitted field is characterized by the normalized second-order autocorrelation function at zero time delay $g^{(2)}(0) = P_{\text{TR}} P_{\text{G}}/P_{\text{T}} P_{\text{R}}$, where P_{T} and P_{R} represent the photon counts in each SPCM, P_{TR} is the coincidence between the two SPCMs, and P_{G} records the total experimental trial gates. Since this work focuses on the autocorrelation function at zero time delay, from now on we define $g^{(2)}(0)$ as $g^{(2)}$.

In theory, the two-particle spin-wave correlation function $g^{(2)}(T_s) \equiv \langle \hat{S}_{\mathbf{k}_0}^\dagger \hat{S}_{\mathbf{k}_0}^\dagger \hat{S}_{\mathbf{k}_0} \hat{S}_{\mathbf{k}_0} \rangle / \langle \hat{S}_{\mathbf{k}_0}^\dagger \hat{S}_{\mathbf{k}_0} \rangle^2$ is given by

$$g^{(2)}(T_s) = \frac{\sum_{m\geqslant 2} |c_m|^2 m(m-1) X_m(T_s)}{|\sum_{m\geqslant 1} |c_m|^2 m Y_m(T_s)|^2}, \qquad (1)$$

where we define $X_m = \frac{1}{m(m-1)} \langle \mathbf{m}|\hat{U}^\dagger \hat{S}^\dagger \hat{S}^\dagger \hat{S}\hat{S}\hat{U}|\mathbf{m}\rangle$ and $Y_m = \frac{1}{m} \langle \mathbf{m}|\hat{U}^\dagger \hat{S}^\dagger \hat{S}\hat{U}|\mathbf{m}\rangle$. Our numerical modeling is based on Monte Carlo simulations for atoms randomly sampled according to a three-dimensional Gaussian density. The runtimes required for the simulations scale as N^m when we sum over the m-body phase shifts. In order to reduce the computation complexity, the maximum value of m used in Eq. (1) is truncated at $m = M$. In Fig. 1(c), $g^{(2)}(T_s = 0)$ is shown as a function of M (the right y axis). The results suggest that, in order to properly account for multiple excitations in calculating $g^{(2)}(T_s = 0)$, values of $M \geqslant 7$ should be used. Because the Monte Carlo simulation for $m \geqslant 5$ is computationally intensive, we also use an ansatz for large N where we set $X_m = X_2^{2m-3}$ and $Y_m = Y_2^{m-1}$, in which case the runtime scales only as N^2. The approximation works surprisingly well when compared with the exact solution, with the details provided in the Supplemental Material [27].

To look into the generation of single photons out of an initially unentangled multiexcitation state, we measure $g^{(2)}(T_s)$ as a function of storage time, shown in Fig. 2. We observe an evolution for the retrieved field from a coherent state ($g^{(2)} = 1$) to a single-photon state ($g^{(2)} = 0$) for $n = 50$ (green closed squares in Fig. 2). When the interaction strength is
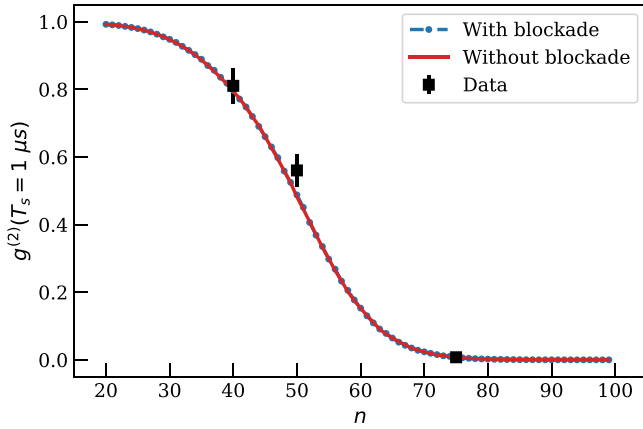
FIG. 3. Plot of $g^{(2)}(T_s = 1 \mu s)$ as a function of principal quantum number n with the effect of blockade (orange dashed line) and without the effect of blockade (blue solid line). Experimental data for $n = 40, 50,$ and 75 are shown by black squares.

reduced by exciting to a lower Rydberg state, i.e., $n = 40$, the dephasing rate is respectively lower (orange closed circles in Fig. 2). For the numerical simulation shown as solid lines in Fig. 2, the excited state is truncated at $M = 50$. The parameters $\sigma_x = \sigma_y = 5.85 \mu m$ are determined from the beam waist of the excitation field E_1, while σ_z is used as a free parameter to fit the two curves, with $\sigma_z = 10.5 \mu m$ providing the lowest mean square error [27].

The dephasing rate is also a function of the atom sample size. The larger longitudinal length will result in larger average distances between atoms, leading to slower dephasing. We control the sample size experimentally by changing the loading scheme: If atoms are loaded from the MOT to the FORT and then to the SILT, a (short) sample of $\sigma_z = 10.5 \mu m$ is created, whereas when atoms are loaded into the SILT directly from the MOT, a (long) pencil-shaped sample with length of 1 mm is achieved. The size of the ensemble undergoing excitation is determined by the Rayleigh range of the E_1 field $z_{R,1} \approx 135 \mu m$, from which we extract $\sigma_z = \sqrt{2/\ln 2} z_{R,1} \approx 230 \mu m$ for the theory simulations. The data and simulations are in agreement with $g^{(2)} \approx 1$ for the long ensemble (green open squares in Fig. 2).

In these experiments, the Rydberg blockade effect is playing a minor role in the excitation phase. One way to justify this assertion is as follows: The excitation blockade occurs when the interaction strength between Rydberg atoms exceeds both the Rabi frequency and bandwidth of the laser excitation, with the blockade radius (approximately) given by $R_b = [C_6/\hbar \max(\Omega, 1/T_p)]^{1/6}$, with $C_6 = h \times 15.44 \, (1.00) \, GHz \, \mu m^6$ for $n = 50 \, (40)$ [28]. Since in our

experiment $\Omega < 1/T_p$, the blockade radius is determined by the pulse duration and estimated to be 4.6 and 2.9 μm for principal quantum numbers of $n = 50$ and 40, respectively (see Ref. [27] for details). This corresponds to a maximum of seven excitations for $n = 50$ and 28 excitations for $n = 40$. Since the average number of Rydberg excitations $\bar{m} = 1.63 \, (0.79)$ for $n = 40 \, (50)$ is much smaller than the maximum numbers given above, the blockade is expected to play a negligible role.

As another justification that the observed reduction of measured $g^{(2)}$ for all storage times can be assigned to the dephasing, as opposed to being a result of the excitation blockade during the excitation phase, we model the effects of the blockade by excluding from the simulation pairs of atoms whose distance from each other is less than the blockade radius R_b. We compare these values to those where $g^{(2)}$ is computed including all atom pairs. In Fig. 3 $g^{(2)}(T_s = 1 \mu s)$ is plotted as a function of principal quantum number n with the blockade effect (orange dashed line) and without the blockade (blue solid line). There is no discernible difference between the two curves and they agree with the experimental data (black squares). Further analysis given in the Supplemental Material suggests that it is a general feature that the excitation blockade does not contribute to the observed value of $g^{(2)}$ at times longer than the duration of excitation pulse, something that happens by default in the excitation-and-retrieval types of ensemble experiments [27].

In summary, we have demonstrated clearly the effect of dynamic dephasing on spin-wave correlations. The dephasing results from phase shifts associated with Rydberg atom–Rydberg atom interactions. To explain the results, we developed a computationally efficient Rydberg-Rydberg interaction dephasing theory model that agrees well with the exact solution. By varying the interaction time from 0.1 to 25 μs, we measured the autocorrelation function $g^{(2)}$ of the phase-matched retrieval photons using a HBT setup and observed a fast transition of $g^{(2)}$ from 1 to 0 for low principal quantum numbers, i.e., $n = 40$ and 50, showing the single-photon property. For our experimental conditions, the Rydberg blockade has been shown to have a negligible effect on the results. Our approach not only provides an ideal platform to compare the blockade and dephasing mechanism, but also has implications for optimizing efficiency, speed, and error probability of on-demand single-photon generation and manipulation.

[1] M. D. Lukin, M. Fleischhauer, R. Cote, L. M. Duan, D. Jaksch, J. I. Cirac, and P. Zoller, Dipole Blockade and Quantum Information Processing in Mesoscopic Atomic Ensembles, Phys. Rev. Lett. **87**, 037901 (2001).

[2] M. Saffman, T. G. Walker, and K. Mølmer, Quantum information with Rydberg atoms, Rev. Mod. Phys. **82**, 2313 (2010).

[3] H. Labuhn, D. Barredo, S. Ravets, S. de Léséleuc, T. Macri, T. Lahaye, and A. Browaeys, Tunable two-dimensional arrays

of single Rydberg atoms for realizing quantum Ising models, Nature (London) **534**, 667 (2016).

[4] S. Ebadi, A. Keesling, M. Cain, T. T. Wang, H. Levine, D. Bluvstein, G. Semeghini, A. Omran, J.-G. Liu, R. Samajdar, X.-Z. Luo, B. Nash, X. Gao, B. Barak, E. Farhi, S. Sachdev, N. Gemelke, L. Zhou, S. Choi, H. Pichler *et al.*, Quantum optimization of maximum independent set using Rydberg atom arrays, Science **376**, 1209 (2022).

[5] T. M. Graham, Y. Song, J. Scott, C. Poole, L. Phuttitarn, K. Jooya, P. Eichler, X. Jiang, A. Marra, B. Grinkemeyer, M. Kwon, M. Ebert, J. Cherek, M. T. Lichtman, M. Gillette, J. Gilbert, D. Bowman, T. Ballance, C. Campbell, E. D. Dahl *et al.*, Multi-qubit entanglement and algorithms on a neutral-atom quantum computer, Nature (London) **604**, 457 (2022).

[6] D. Bluvstein, H. Levine, G. Semeghini, T. T. Wang, S. Ebadi, M. Kalinowski, A. Keesling, N. Maskara, H. Pichler, M. Greiner, V. Vuletić, and M. D. Lukin, A quantum processor based on coherent transport of entangled atom arrays, Nature (London) **604**, 451 (2022).

[7] M. Saffman and T. G. Walker, Creating single-atom and single-photon sources from entangled atomic ensembles, Phys. Rev. A **66**, 065403 (2002).

[8] Y. Miroshnychenko, U. V. Poulsen, and K. Mølmer, Directional emission of single photons from small atomic samples, Phys. Rev. A **87**, 023821 (2013).

[9] D. Petrosyan and K. Mølmer, Deterministic Free-Space Source of Single Photons Using Rydberg Atoms, Phys. Rev. Lett. **121**, 123605 (2018).

[10] T. Stolz, H. Hegels, M. Winter, B. Röhr, Y.-F. Hsiao, L. Husel, G. Rempe, and S. Dürr, Quantum-Logic Gate between Two Optical Photons with an Average Efficiency above 40%, Phys. Rev. X **12**, 021035 (2022).

[11] D. Tiarks, S. Schmidt-Eberle, T. Stolz, G. Rempe, and S. Dürr, A photon-photon quantum gate based on Rydberg interactions, Nat. Phys. **15**, 124 (2019).

[12] Y. Mei, Y. Li, H. Nguyen, P. R. Berman, and A. Kuzmich, Trapped Alkali-Metal Rydberg Qubit, Phys. Rev. Lett. **128**, 123601 (2022).

[13] J. Vaneecloo, S. Garcia, and A. Ourjoumtsev, Intracavity Rydberg Superatom for Optical Quantum Engineering: Coherent Control, Single-Shot Detection, and Optical π Phase Shift, Phys. Rev. X **12**, 021034 (2022).

[14] F. Bariani, Y. O. Dudin, T. A. B. Kennedy, and A. Kuzmich, Dephasing of Multiparticle Rydberg Excitations for Fast Entanglement Generation, Phys. Rev. Lett. **108**, 030501 (2012).

[15] Y. O. Dudin and A. Kuzmich, Strongly interacting Rydberg excitations of a cold atomic gas, Science **336**, 887 (2012).

[16] Y. O. Dudin, F. Bariani, and A. Kuzmich, Emergence of Spatial Spin-Wave Correlations in a Cold Atomic Gas, Phys. Rev. Lett. **109**, 133602 (2012).

[17] L. Li, Y. O. Dudin, and A. Kuzmich, Entanglement between light and an optical atomic excitation, Nature (London) **498**, 466 (2013).

[18] L. Li and A. Kuzmich, Quantum memory with strong and controllable Rydberg-level interactions, Nat. Commun. **7**, 13618 (2016).

[19] H. Busche, P. Huillery, S. W. Ball, T. Ilieva, M. P. A. Jones, and C. S. Adams, Contactless nonlinear optics mediated by long-range Rydberg interactions, Nat. Phys. **13**, 655 (2017).

[20] Y. O. Dudin, L. Li, F. Bariani, and A. Kuzmich, Observation of coherent many-body Rabi oscillations, Nat. Phys. **8**, 790 (2012).

[21] D. P. Ornelas-Huerta, A. N. Craddock, E. A. Goldschmidt, A. J. Hachtel, Y. Wang, P. Bienias, A. V. Gorshkov, S. L. Rolston, and J. V. Porto, On-demand indistinguishable single photons from an efficient and pure source based on a Rydberg ensemble, Optica **7**, 813 (2020).

[22] J. Lampen, H. Nguyen, L. Li, P. R. Berman, and A. Kuzmich, Long-lived coherence between ground and Rydberg levels in a magic-wavelength lattice, Phys. Rev. A **98**, 033411 (2018).

[23] H. Nguyen, J. Lampen, P. R. Berman, and A. Kuzmich, Differential nuclear-spin-dependent light shifts and state mixing of Rydberg atoms, Phys. Rev. A **100**, 033412 (2019).

[24] E. A. Goldschmidt, D. G. Norris, S. B. Koller, R. Wyllie, R. C. Brown, J. V. Porto, U. I. Safronova, and M. S. Safronova, Magic wavelengths for the $5s$–$18s$ transition in rubidium, Phys. Rev. A **91**, 032518 (2015).

[25] J. Stanojevic, V. Parigi, E. Bimbard, A. Ourjoumtsev, P. Pillet, and P. Grangier, Generating non-Gaussian states using collisions between Rydberg polaritons, Phys. Rev. A **86**, 021403(R) (2012).

[26] F. Bariani, P. M. Goldbart, and T. A. B. Kennedy, Dephasing dynamics of Rydberg atom spin waves, Phys. Rev. A **86**, 041802(R) (2012).

[27] See Supplemental Material at http://link.aps.org/supplemental/10.1103/PhysRevA.106.L051701 for the detailed calibration of experimental parameters, the derivation of the dephasing dynamics for multiply Rydberg excitations, and the discussion of the Rydberg blockade effect in our system.

[28] N. Šibalić, J. D. Pritchard, C. S. Adams, and K. J. Weatherill, ARC: An open-source library for calculating properties of alkali Rydberg atoms, Comput. Phys. Commun. **220**, 319 (2017).